EXPLORING THE PRINCIPLES OF A PRIMAL MAGNETIC MILL

J.L. Duarte
Dept. Electrical Engineering (Ret.)
Eindhoven University of Technology
The Netherlands

(Dated: 02 June 2026)

Abstract

Magnetic-wind mills use magnetic forces to perform mechanical work. This report presents a methodology for the analysis and synthesis of an unadorned magnet-only mill designed to enable continuous power harvesting from, arguably, the spacetime background. Experimental results from a working prototype are also presented, showing a mill that reduces the electric power input of a test system, yielding relative energy performance rates up to 114%, which serves as the basis for the discussion and analysis in this report.

I. Archetypes

There are countless videos online promoting so-called ”free-energy” devices. However, it goes without saying that so long as no detailed instructions are correctly provided on how to reproduce these devices independently, people are tricked into claims which do not attach to any valid scientific method.

Astonishingly, among the multitude of obscure free-energy showcases that *www* archaeology allows us to unearth on the Internet, there is a shining spot: it is just a plastic bottle, fully transparent, supporting a structured array of small permanent-magnet discs, illustrated in Fig. 1. The demonstration shows that when the stator vanes approach the rotor, the bottle begins to spin, and keeps going on without recurrence to other everyday external excitation!

Since friction losses, although quite low, are inevitable during spinning, the research question in what follows is *where the required mechanical power to overcome friction springs from*?

Fig. 1: Still taken from a demonstration video previously available on the Internet, as provided by an anonymous inventor [1].

An explanation for the working principle of the device in Fig. 1 can *not* be found from present-time Standard Model of Physics.[1] Even so, we show in the sequence that similar outcomes as recorded in [1] can be *well* reproduced.

In Section II we propose the concept for a minimalist magnetic mill, akin to the setting in Fig. 1, and present results of test measurements taken from a laboratory setup with the accomplished prototype. Performance assessment confirms excess power generation. In Section III we propose a modeling approach for this primal mill, to give a theoretical frame for the experimental findings, on the grounds of a Unified Physics Theory [2] and a vibrational model for magnetic-wind mills in [3]. Subsequently, aiming at further research and design improvement, we discuss tools for analysis and synthesis in Sections IV and V, respectively. In Section VI, we address a procedure on how to optimize the design, and include also technical data of the built test platform. Finally, we draw conclusions in Section VII.

[1] If you, dear reader, were to question where the seminal ideas behind inventing inusitated gadgets as in Fig. 1 come from, challenging the rules of Classical Electromagnetism, we would venture to quote – who else? – a poet: *”Deus quer, o homem sonha, a obra nasce.”* (”God wills it, man dreams, the work is born.”) - F. Pessoa, *Mensagem*, 1935.

II. First things first: Experiments

A. Minimalist concept

We intend to explore a stripped-down magnetic mill as shown in Fig. 2, as proof of concept for the essential aspect claimed in Fig. 1 that is *generation of mechanical power*.

This primal mill is assembled with disc-shaped permanent magnets only, for which the design parameters are defined in Figs. 3 and 4, to be used in the sequel. The mill is not expected to show self-rotating characteristics as in [1]. Nonetheless, the existence of excess energy within a test setup must be confirmed through measurements while the magnetic mill is driven into rotation.

The optimal choice of disc PM components and parameter values for a test prototype is detailed later in Sec. VI.

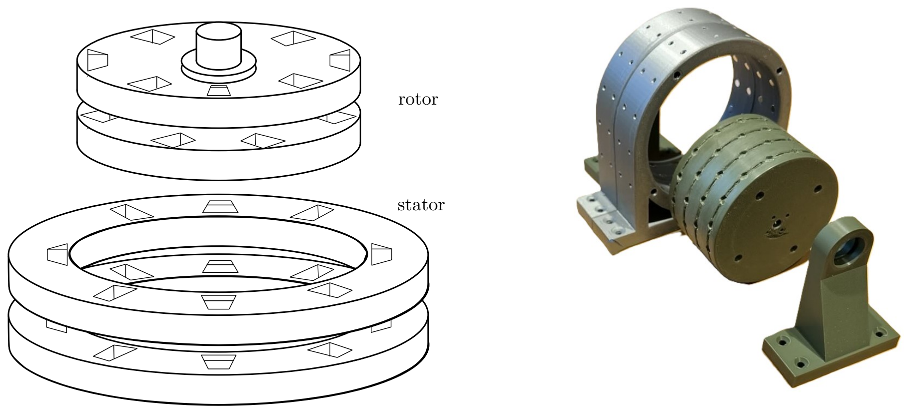

(a) Exploded view; $\eta = 8$.

(b) 3D-printed parts for $\eta = 16$.

Fig. 2: Primal magnetic mill parts, with helicoidally staggered rotor rings. Both ring types have the same η, the amount of disc PMs per ring.

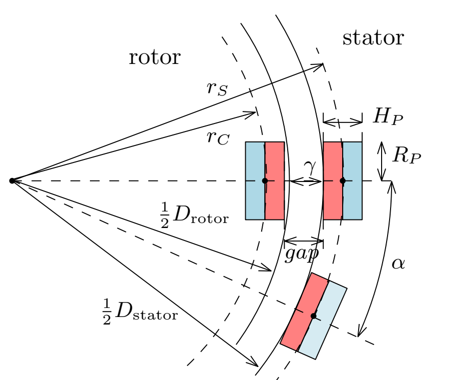

η disc PMs $-$ (D_P, H_P)

$\alpha = 2\pi/\eta \qquad R_P = \frac{1}{2}D_P$

$r_S = r_C + H_P + gap$

$D_{\text{rotor}} = 2\sqrt{(r_C + \frac{1}{2}H_P)^2 + R_P^2}$

$D_{\text{stator}} = 2\,(r_C + \frac{1}{2}H_P + gap)$

$\gamma = \frac{1}{2}(D_{\text{stator}} - D_{\text{rotor}})$

$\gamma \approx gap - \frac{R_P^2}{2(r_C+(1/2)H_P)}$ when $R_P << r_C$

Fig. 3: Rotor and stator with face-to-face magnets – geometrical quantities. It should be noted that D_{rotor} is the outer diameter of the rotor, D_{stator} the inner diameter of the stator, and gap the face-to-face separation between magnets.

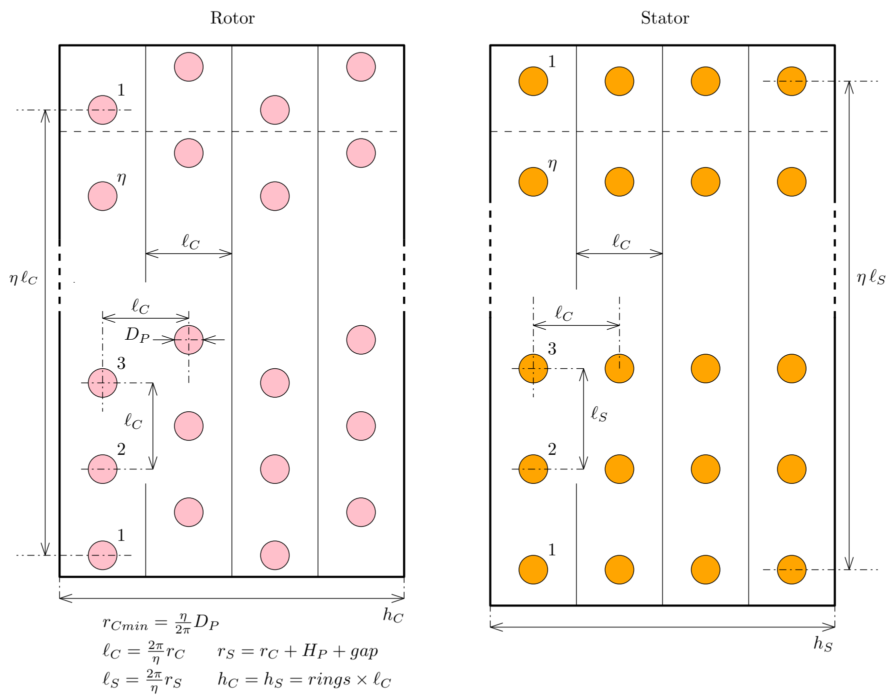

Fig. 4: Flat view of stator and staggered rotor rings. The height of the rotor cylinder, h_C, is determined by the interval ℓ_C between rotor magnets.

B. Test platform

Fig. 5 shows the diagram representation of a platform that allows conducting experiments with the primal mill.

The prime mover is a BLDC motor, equipped with electronic driver and adjustable speed control, having electric power input from a stabilized DC voltage supply. The DC current taken from the supply (sensor ”A”) is a measure of the system total electric power input to feed the BLDC motor and to surpass all possible system losses, including mechanical friction, in order to put the magnetic mill at a desired rotational speed (sensor ”rpm”).

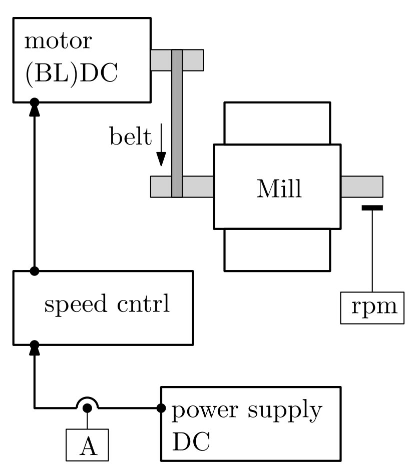

Fig. 5: Setup for test purposes. A BLDC motor is the prime mover that drives the magnetic mill by means of a belt.

Fig. 6 illustrates the laboratory setup to test an assembled mill prototype, whose design parameters are listed in Table III (Sec. VI).

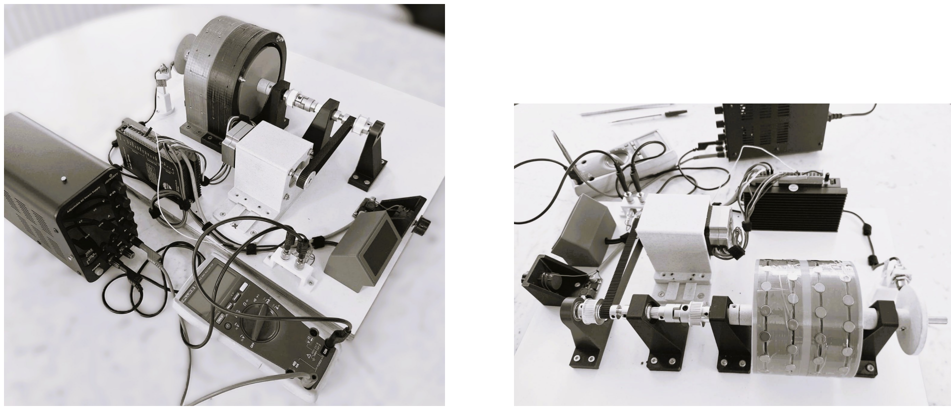

(a) Mill with rotor and stator. (b) Incomplete mill with rotor only.

Fig. 6: Platform for testing a primal magnetic mill. Technical details of the key components are listed in Fig. 13.

C. Measurements

In Table I, two data arrays are shown with the measured current drawn from the power supply at constant voltage of 24VDC, concerning the magnetic mill without and with stator, respectively, as function of the rotational speed. Thereafter, Table II displays the resultant total system electric power input as inferred from Table I.

For the case of an incomplete magnetic mill with rotor only, the acquired DC current data provide a reference for quantifying the total losses in the system as function of the rotational speed, which include electric losses in the BLDC motor and companion electronic driver, mechanical friction on the bearings and belt, windage friction of the rotor against air, and power supply of ancillary sensors.

Once the magnetic mill is fully assembled, including the stator, we would generally expect the total system losses to increase. First, the BLDC driver must exert additional effort to overcome the cogging torque generated by the magnetic

TABLE I: Measured output DC current at constant regulated 24 VDC supply, as function of the rotational speed. (Mill parameters listed in TABLE III.)

Mill	(1) rotor only	(2) with stator
rpm	[A]	[A]
0	0.097	0.097
250	0.170	0.158
500	0.219	0.196
750	0.271	0.239
1000	0.324	0.284
1250	0.377	0.336
1500	0.429	0.388
1750	0.486	0.446
2000	0.542	0.504
2250	0.600	0.567
2500	0.654	0.626
2750	0.713	0.690
3000	0.769	0.754

With stator: gap = 6 mm
Tachometer: 10-9999 rpm (accuracy: 0.10%)
A sensor: FLUKE 179 (resolution: 0.001 ADC)
V supply: JESVERTY SPS-3010V $\rightarrow$ 24 VDC
Stability constant 24 VDC $\leq$ 0.5% +3mV

TABLE II: Power measurements as derived from Table I

Mill	(1)rotor only	(2)with stator	(1) − (2)	(1) ÷ (2)
rpm	$[W]$	$[W]$	P'_S $[W]$	REP
0	2.33	2.33	0	1.00
250	4.08	3.79	+0.29	1.08
500	5.26	4.70	+0.55	1.12
750	6.50	5.73	+0.77	1.13
1000	7.78	6.84	+0.96	1.14
1250	9.05	8.06	+0.98	1.12
1500	10.30	9.32	+0.98	1.11
1750	11.66	10.70	+0.96	1.09
2000	13.01	12.10	+0.91	1.08
2250	14.40	13.61	+0.79	1.06
2500	15.70	15.02	+0.68	1.04
2750	17.11	16.56	+0.55	1.03
3000	18.46	18.10	+0.36	1.02

Excess power generation = difference $[W(1) - W(2)]$
REP - relative energy input performance = $[W(1)/W(2)]$

attraction and repulsion between the rotor and stator magnets. In addition, extra electrical losses arise from eddy currents induced by magnetic flux pulsations in the metallic coatings of both the rotor and stator magnets. Furthermore, the airflow through the rotor–stator gap may transition to a more turbulent regime, thereby increasing windage friction.

Yet, Table II shows that, *unexpectedly*, for the same angular speed, the measured total electric power input for driving a whole magnetic mill (with stator and rotor) is *lower* than in the circumstance with rotor only! As a result, relative energy input performance (REP) greater than one appears in Table II.

D. Remarks

In Fig.7 the results of Table II are visualized. As shown in Fig.7(a), the total electric power taken from the DC voltage supply grows with the rotational speed in both cases. For the incomplete mill with rotor only, the electric power is higher with respect to a fully assembled mill. The difference in total power input, P'_S = col. (1) minus (2), and the energy input relative performance, REP = ratio of col. (1) to (2), are depicted in Figs.7(b) and 7(c).

Under identical rotational speeds, the internal system losses with a fully assembled magnetic mill should not be lower than those observed when operating without the stator. Therefore, a positive value of P'_S in Fig. 7 suggests that power is somehow being generated within the system itself.[2]

In this report, we consider the possibility that P'_S represents an increment of mechanical power added to the shaft of the primal magnetic mill, for which we assume that the required energy source is unfolded from resonance in quantum vacuum fields. More specifically, the region of linear growth of P'_S in Fig. 7(b) gives a hint where the extra energy could come from, and P'_S is analyzed and *calculated* in the sequence from a theoretical point of view.

[2] An attentive reader might point out that the observed effect could stem from an anomaly in the electronic driver used. To verify this possibility we performed repeated measurements, including reversing the shaft rotational direction, and the results remained essentially unchanged. In case of malfunction, random noise in P'_S would be expected, rather than regularly acquired positive values.

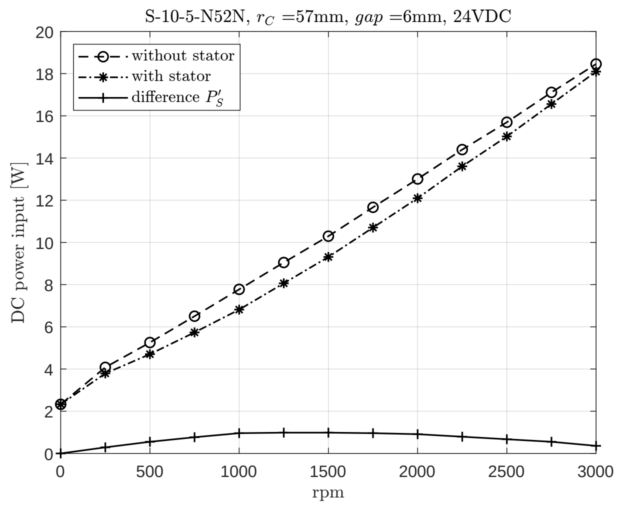

(a) Magnetic mill with and without stator.

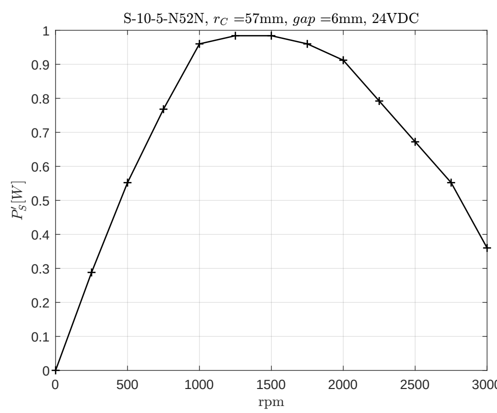

(b) System power input difference

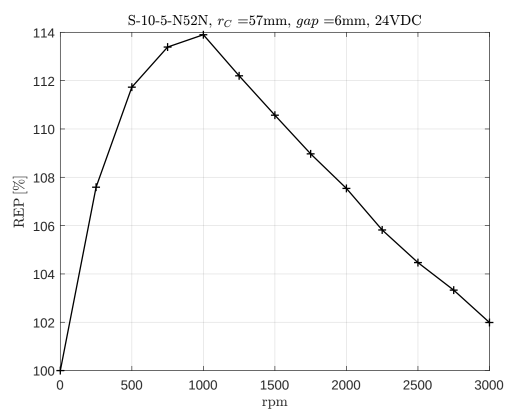

(c) Energy input relative performance

Fig. 7: (a) Power measurements from Table II. (b) The difference in power input, P'_S, which would initially be expected to be negative but was instead measured to be positive, must be supplied by an additional energy source in order to maintain the same rotational speed in both configurations. (c) Relative performance rates up to 114%, meaning that, with a fully assembled mill, 14% less electric power input into the test system is needed for the same rotational speed.

III. Fundamentals of Modeling

As noted before, in Fig. 7(b) firstly P'_S increases linearly proportional to the rotational speed, up to about 1000 rpm. Then, it enters in nonlinear decay.

The linear behavior of P'_S in the lower speed region is appealing for further research, because the internal losses of the system in both configurations (with and without the stator) remain close to one another.[3] Therefore, as long as the differential measurements cancel nearly equivalent total system losses, what remains is the uncovered nature of the internal generated power, which is directly proportional to the rotational speed.

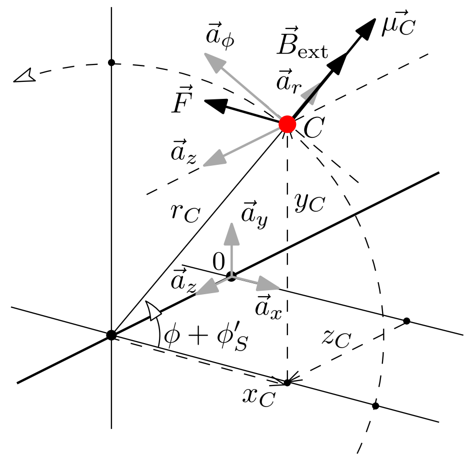

Fig. 8: Magnetic dipole moment $\vec{\mu}_C$, which represents a disc-shaped permanent magnet (PM) as located in the rotor rings of Fig. 2, interacting with an external radial magnetic field, $\vec{B}_{\text{ext}}$, under mechanical angular vibrations ϕ'_S.

Building on the vibrational model in [3] and starting from Fig. 8, our goal is to calculate P'_S as the mechanical power added to the shaft of the primal magnetic mill[4], on the basis of

$$\vec{F} = \vec{\nabla}(\vec{B}_{\text{ext}} \cdot \vec{\mu}_C) = F_r\,\vec{a}_r + F_\phi\,\vec{a}_\phi, \quad (1)$$

$$\vec{B}_{\text{ext}} = \left(B_S + B'_S\cos(\eta\phi)\right)\vec{a}_r, \quad (2)$$

$$d\phi'_S = \lambda\frac{\partial F_r}{\partial \phi}d\phi. \quad (3)$$

Regarding (1), the force $\vec{F}$ on $\vec{\mu}_C$ is due to the gradient of the inner product with $\vec{B}_{\text{ext}}$ from (2), which is a radial field with amplitude modulation $B'_S\cos(\eta\phi)$ on top of a carrier B_S. The component $B'_S\cos(\eta\phi)$ is created by the stator magnets, while the component B_S is part of a surrounding magnetic field, for which circularly polarized waves with Beltrami-like structure are evoked from resonance in quantum vacuum fields, owing to matched disturbances [2, Sec. 5.4.4]. The pulsating attraction/repulsion interaction of the rotor magnets with the stator rings places inherently synchronized disturbances in the helicoidal magnetic field gradient in Fig. 2 (in a like manner as in Fig. 1).

As a result of created impulsive forces in the structure, incremental angular disturbances $d\phi'_S$ are triggered in the rotating shaft, being linearly correlated (coefficient λ in (3)) to the rate-of-change of F_r, the radial component of $\vec{F}$. We introduce this correlation as a fundamental hypothesis underlying the proposed

[3]Friction, windage and parasitic losses increase more significantly at higher angular speeds.

[4]The value of P'_S is found after manipulations yielding to Eq.(13).

modeling approach. Accordingly, the numerical value of λ is all we need for substantiating the link with the evoked surrounding magnetic field B_S as a source of energy coming from vacuum fluctuations.

The specific magnetic materials and geometry of the mill assemblage, together with the matched field disturbances, determine an empirical value for λ. Fortunately, we can readily identify λ from simple power measurements, as discussed in Section V.

In the low-speed range of Fig. 7(b), where P'_S linearly increases proportional to the angular rotation, the coefficient λ is practically invariant. However, λ becomes a variable function of the speed at higher spinning operation, possibly due to changes in the synchronizing disturbances in conjunction with higher system losses, resulting in nonlinear decay of P'_S beyond 1000 rpm.[5]

Owing to the resultant angular vibrations ϕ'_S from (3), staying mechanical power might conceivably be explained as scavenged from quantum vacuum fields and delivered to the spinning mill shaft.

[5]We limit the scope of this report to the linear behavior of P'_S, leaving the nonlinear characteristics to be explored in subsequent research.

IV. Tools for analysis

References to relevant equations from Part III in [3] are given in the form Eq.$(III.\mathrm{xx})$. The same definitions for symbols are used herein. In addition, Tables I and II of Sec. VI list together all parameters and geometric quantities.

A. Impulsive radial force

Once the magnitude B'_S in (2) is quantified[6], we can write in compliance with Eq.$(III.23)$ that

$$\frac{\partial F_r}{\partial \phi} = F_0\,\Gamma(\phi)\,, \quad \text{where} \tag{4}$$

$$F_0 = 2\frac{\eta\mu_C B'_S}{r_C}\,, \quad \text{and} \tag{5}$$

$$\Gamma(\phi) = \frac{-1}{\sin(2\phi)}\left(2\frac{\sin(\eta\phi)}{\sin(2\phi)} - \eta\cos(\eta\phi)\cos(2\phi)\right). \tag{6}$$

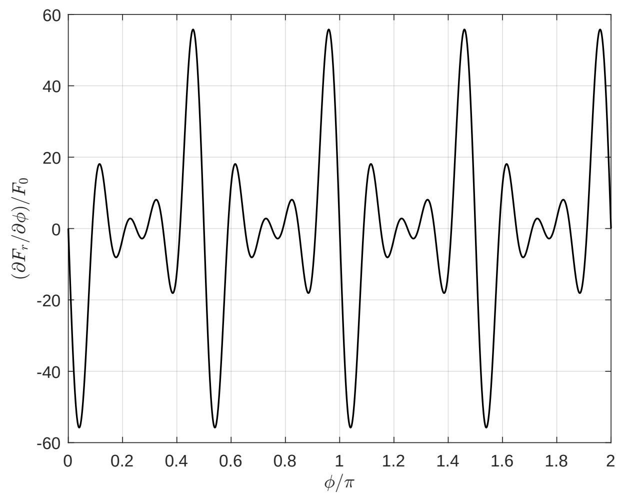

Fig. 9: Normalized $\Gamma(\phi)$ in (6) with $\eta = 16$. It results in $\textsc{max}\{\Gamma(\phi)\} = 56$.

As shown in Fig. 9, the impulsive nature of $\Gamma(\phi) = \frac{1}{F_0}(\partial F_r/\partial\phi)$, the normalized angular rate-of-change of F_r, is a characteristic of magnetic mills [4]. It is impressed by η, the amount of PMs in each stator/rotor ring.

B. Angular disturbances

Respecting Eq.$(III.22)$, from (3) and (4) follows

$$\frac{d\phi'_S}{d\phi} = \lambda\,F_0\,\Gamma(\phi)\,. \tag{7}$$

Because F_0 and $\Gamma(\phi)$ are already addressed, hence also $\textsc{max}\,\{\Gamma(\phi)\}$, in an attempt to obtain the value of coefficient λ, we can alternatively write relation (7) in a form that proves convenient in subsequent discussions as

$$\lambda = \frac{1}{F_0}\frac{\textsc{max}\{d\phi'_S/d\phi\}}{\textsc{max}\,\{\Gamma(\phi)\}}. \tag{8}$$

where $\textsc{max}\{d\phi'_S/d\phi\}$ is a quantity to be identified (Sec. V). In (8) we intrinsically consider that λ is constant with respect to the angular position ϕ, but its value may vary as function of the shaft rotational speed.

[6]Calculated back-and-forth with Eq.(29).

C. Energy increments

Per each shaft revolution, the energy increment owing to just one single disc magnet in the rotor rings is found from Eqs.$(III.28)\&(III.30)$ to be

$$
\begin{aligned}
Q'_S &= Q_0\,\Psi\,, \qquad \text{with} & (9)\\
Q_0 &= 8\frac{\lambda(\eta\mu_C B'_S)^2}{r_C}, \quad \text{and} & (10)\\
\Psi &= \int_0^{2\pi} \frac{\sin(\eta\phi)}{\sin(2\phi)}\left(2\frac{\sin(\eta\phi)}{\sin(2\phi)} - \eta\cos(\eta\phi)\cos(2\phi)\right) d\phi\,. & (11)
\end{aligned}
$$

Similar to (6), Ψ depends only on η. For instance, in case of $\eta = 16$, it follows from (11) that $\Psi = 50.3$.

D. Power generation

Substitution of (5) and (8) into (9) leads to

$$Q'_S = 4\frac{\Psi\,\eta\,\mu_C B'_S}{\text{MAX}\,\{\Gamma(\phi)\}}\,\text{MAX}\{d\phi'_S/d\phi\}. \qquad (12)$$

Taking into account all disc PMs in the rotor *rings*, the mechanical power added to the shaft is then found to become

$$P'_S = (rings \cdot \eta)\,Q'_S\,\omega \text{ [W]} \qquad (13)$$

with, for uniform circular motion,

$$\omega = \frac{d\phi}{dt} = \frac{2\pi}{60} rpm\,. \qquad (14)$$

So, when $\text{MAX}\{d\phi'_S/d\phi\}$ is invariant regarding the shaft rotation, hence also Q'_S, the expected generated power from (13) should grow linearly with ω, the rotor angular velocity, which is quite in agreement with the measured results for the low-speed range shown in Fig. 7(b). Consequently, the region of validity for the proposed design approach can be easily verified or falsified by experiments.

V. Tools for synthesis

A. Ad-hoc choices

Targeting to a mill prototype design, first the quantities

$$\text{MAX}\{d\phi'_S/d\phi\} = 0.20\times10^{-3}\cdots0.30\times10^{-3} \quad (15)$$

$$\text{disc type PM} \Rightarrow B_{\text{rem}},\,(D_P,H_P)\to\mu_C \quad (16)$$

$$\eta \Rightarrow \Psi,\,\max\{\Gamma(\phi)\},\,\alpha=2\pi/\eta \quad (17)$$

should be assumed. Then, the parameters

$$r_C,\; gap,\; rings,\; rpm$$

can be explored aiming at calculating and determining optimal values for B'_S in (29) and, consequently, for P'_S in (13).

Note that $\text{MAX}\{d\phi'_S/d\phi\}$ is not precisely known *a priori*. Hence, we should confirm it *a posteriori* from experimental results. The value range in (15) is a hint from practical experience with other prototypes, as commented in the following.

B. Missing link

Recall from [3] that $d\phi'_S$ in (3) is hypothesized to be a *disturbance* on the incremental angle $d\phi$, brought about by resonance in quantum vacuum fields, as a result of the assembly geometry. Parameter λ in (8), which value is related to $\text{MAX}\{d\phi'_S/d\phi\}$, is the link to vacuum fluctuations as the extra energy source for the primal magnetic mill.

After assembling a test prototype, the assumed value for $\text{MAX}\{d\phi'_S/d\phi\}$ should be confirmed and, in case of unacceptable mismatch, tuned with the aid of experimental results.

For this purpose, the clue is to reformulate (12) and (13) as

$$\text{MAX}\{d\phi'_S/d\phi\} = \frac{1}{rings}\cdot\left(\frac{\text{MAX}\,\{\Gamma(\phi)\}}{4\Psi\,\eta^2\mu_C\,B'_S}\right)\cdot\left(\frac{P'_S}{\omega}\right), \quad (18)$$

and to register *measured* values of P'_S as function of angular speed ω, like in Table II, from which the rate (P'_S/ω) is obtained. This ratio remains quite invariant at lower rotational speeds, therefore the value of $\text{MAX}\{d\phi'_S/d\phi\}$ can be readily calculated from (18), to serve as basis for subsequent redesign. Moreover, it is expected that $\text{MAX}\{d\phi'_S/d\phi\}$ also remains approximately the same for comparable helix configurations with the proportions shown in Fig.4.

C. B-field calculation

The sketch in Fig. 10 illustrates the circular path to follow for a rotor PM when crossing along adjacent stator PMs, as in Fig. 2. As an aside, a minimum allowed value for radius r_C is

$$r_C > r_C^{\min} = \frac{R_P}{\tan(\alpha/2)} + \frac{H_P}{2}\,. \quad (19)$$

To take advantage of the axisymmetry of disc magnets, the relative position (ρ,h) with respect to PM_1 in Fig. 10 is found to be, for $0<\varphi<\alpha$:

$$h_0 = H_P + gap\,, \quad (20)$$

$$h = h_0 + 2r_C\sin^2(\varphi/2)\,, \quad (21)$$

$$\rho = 2r_C\sin(\varphi/2)\cos(\varphi/2)\,. \quad (22)$$

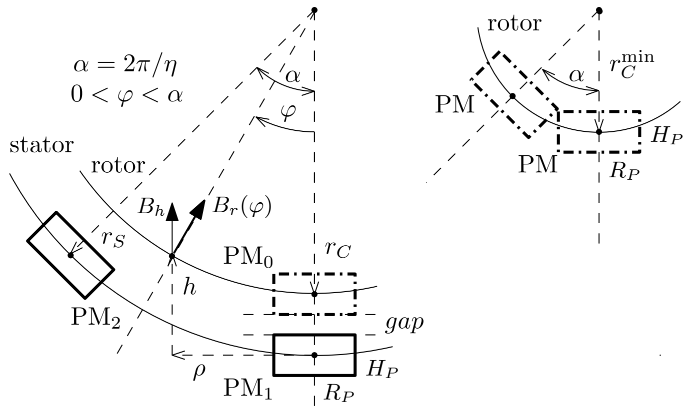

Fig. 10: Rotor (PM_0) and stator (PM_1 and PM_2) magnets. The resultant radial magnetic field $B_r(\varphi)$ at position (ρ, h) is due to the two adjacent stator magnets.

The resultant radial field $B_r(\varphi)$ at (ρ, h), created by linear superposition of B-fields from PM_1 and PM_2, is a constituent part of $\vec{B}_{\text{ext}}$ in Fig. 8. It is given by

$$B_r(\rho, h) = B_{r@\mathrm{PM1}} + B_{r@\mathrm{PM2}}\,, \tag{23}$$

where $B_{r@\mathrm{PM1}}$ (and *mutatis mutandis* $B_{r@\mathrm{PM2}}$) can be calculated via vector potential A_ψ [5] as :

$$\begin{aligned}
B_{r@\mathrm{PM1}} &= B_h(\rho, h)\cos(\varphi), && (24)\\
B_h(\rho, h) &= \frac{A_\psi}{\rho} + \frac{\partial A_\psi}{\partial \rho}\,, && (25)\\
A_\psi &= \frac{B_{\text{rem}}}{2}\left(G(\rho, h; {}^{H_P}\!/2) - G(\rho, h; {}^{-H_P}\!/2)\right), && (26)
\end{aligned}$$

where

$$\begin{aligned}
G(\rho, h; \zeta) &= \frac{2R_P(h-\zeta)}{r_1}\left(\frac{1}{k^2}(\mathcal{J}_2 - \mathcal{J}_1) + \left(\frac{1}{m^2} - 1\right)(\mathcal{J}_3 - \mathcal{J}_1)\right),\\
r_1 &= \sqrt{(\rho + R_P)^2 + (h-\zeta)^2}\,,\ k^2 = \frac{4\rho R_P}{r_1^2}\,,\ m^2 = \frac{4\rho R_P}{(\rho + R_P)^2}\,,\\
\mathcal{J}_1 &= \int_0^{\pi/2} \frac{d\xi}{\sqrt{1 - k^2\sin^2(\xi)}}\,,\ \mathcal{J}_2 = \int_0^{\pi/2} \sqrt{1 - k^2\sin^2(\xi)}\,d\xi\,,\\
\mathcal{J}_3 &= \int_0^{\pi/2} \frac{d\xi}{\sqrt{1 - k^2\sin^2(\xi)}\,(1 - m^2\sin^2(\xi))}.
\end{aligned}$$

Referring to (21) and (22), ρ and h are functions of φ. Therefore, a first-order approximation for the resulting $B_r(\varphi) \cong B_r(\rho, h)$ in (23) is achieved with

$$B_r(\varphi) \approx B_0 + B_S' \cos(\eta\varphi) \tag{27}$$

for $0 < \varphi < \alpha = 2\pi/\eta$, with

$$B_0 = \frac{1}{\alpha}\int_0^\alpha B_r(\varphi)\,d\varphi\,, \tag{28}$$

and the magnitude B_S' – a quantity required in (5) – is found from

$$B_S' = \frac{2}{\alpha}\int_0^\alpha B_r(\varphi)\cos(\eta\varphi)\,d\varphi\,. \tag{29}$$

As an example, we compare results of (27) in Fig.11.

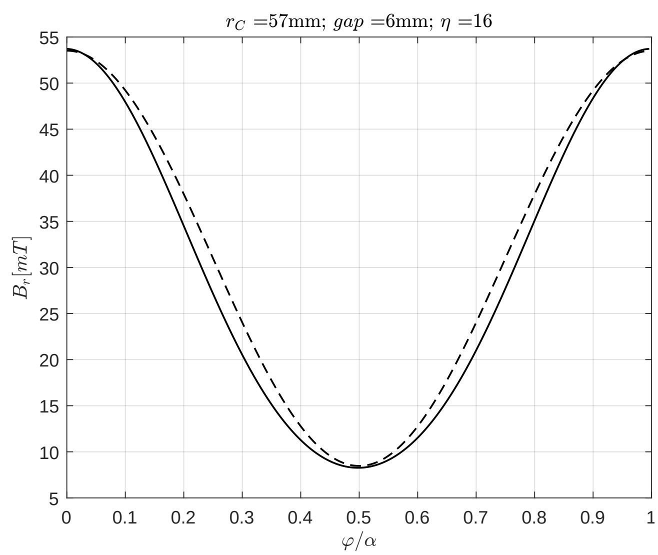

Fig. 11: Close fit of results for B-fields in (27). *Line trace*: $B_r(\varphi)$ analytically calculated with (23); *dashed trace*: $B_0 + B'_S \cos(\eta\varphi)$ from (28)-(29); other parameters in Table III.

VI. HANDS-ON OPTIMIZATION

A. Iteractive attempts

With the purpose of deciding on the parameters of an exemplary mill prototype, we start with the choice of ad-hoc quantities :

- PM S-10-5-N52N : B_{rem} = 1.45T, D_P =10mm, H_P =5mm,
- η = 16 , $rings$ = 4, rpm = 1000,
- $\text{MAX}\{d\phi'_S/d\phi\}$ = 0.244×10^{-3}.

Next, conforming (29), (12) and (13), respectively, the impact on

$$\begin{aligned} B'_S &= f(B_r) \,@\, \text{optimized by manipulation of } r_C \,\&\, gap \\ Q'_S &= f(B'_S) \,@\, \text{parameterized by } \text{MAX}\{d\phi'_S/d\phi\} \\ P'_S &= f(Q'_S, \omega) \,@\, \text{resulting added power to the mill shaft} \end{aligned}$$

can be analyzed iteractively, as illustrated in Fig. 12. The plots reveal the sensitivity to parameters r_C and gap. It can be concluded that the effect of variations in gap are more pronounced than increments in r_C.

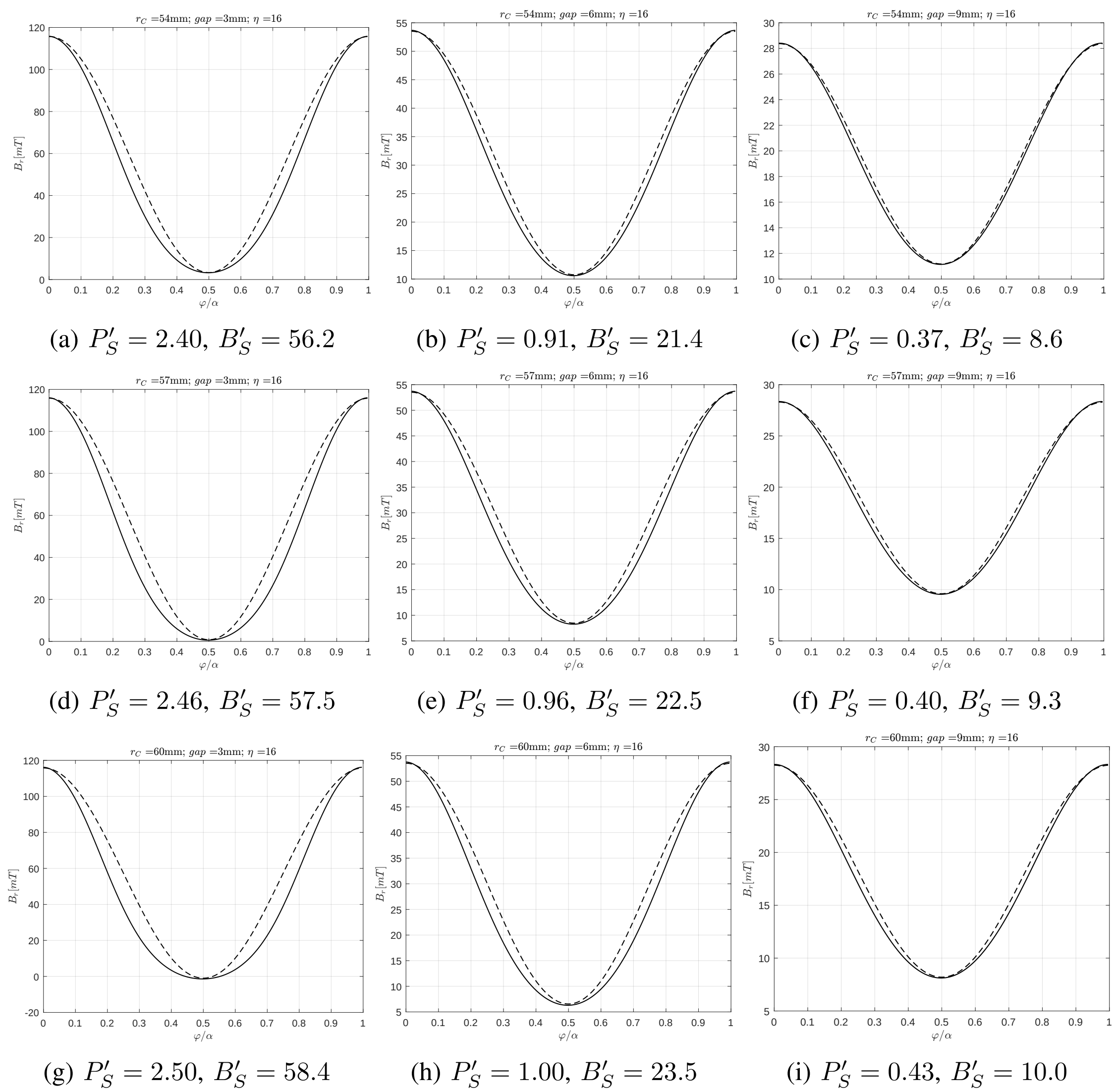

(a) $P'_S = 2.40$, $B'_S = 56.2$ (b) $P'_S = 0.91$, $B'_S = 21.4$ (c) $P'_S = 0.37$, $B'_S = 8.6$

(d) $P'_S = 2.46$, $B'_S = 57.5$ (e) $P'_S = 0.96$, $B'_S = 22.5$ (f) $P'_S = 0.40$, $B'_S = 9.3$

(g) $P'_S = 2.50$, $B'_S = 58.4$ (h) $P'_S = 1.00$, $B'_S = 23.5$ (i) $P'_S = 0.43$, $B'_S = 10.0$

Fig. 12: Exploring $gap = 3/\,6/\,9$ [mm] and $r_C = 54/\,57/\,60$ [mm]; rpm = 1000. *Line trace*: $B_r(\varphi)$; *dashed trace*: $B_0 + B'_S\cos(\eta\varphi)$; P'_S in [W], B'_S in [mT].

B. Implementation

We consider the situation in Fig. 12(e) as a good trade-off for a proof-of-principle prototype, considering size and acceptable cogging torque. The final magnetic mill parameters are listed in Tables III and IV.

TABLE III: Design parameters and geometrical dimensions

Quantity		$Value$	Description
N52	[NeFB]	–	S-10-05-N52N disc PM from Supermagnete
$B_{\rm rem}$	[T]	1.45	remanent magnetization
D_P	[mm]	10.0	PM disc diameter
H_P	[mm]	5.0	PM disc height
R_P	[mm]	5.0	PM disc radius = $0.5D_P$
$rings$	[-]	4	number of rings with PMs in rotor/stator
η	[-]	16	number of PM's per ring - Fig. 2
n_{PM}	[-]	128	total amount of PM's (rotor+stator)
α	[rad]	$2\pi/\eta$	PM angular separation per ring - Fig. 3
gap	[mm]	6.0	face-to-face PM radial spacing - Fig. 3
γ/gap	[-]	0.97	effective free space between PMs - Fig. 3
r_C	[mm]	57	radius from rotor PM center to shaft - Fig. 3
r_S	[mm]	68	radius from stator PM center of shaft - Fig. 3
ℓ_C	[mm]	22	circular spacing between rotor PMs - Fig. 4
ℓ_S	[mm]	27	circular spacing between stator PMs - Fig. 4
h_C	[mm]	67	rotor/stator axial height - Fig. 4
$D_{\rm rotor}$	[mm]	119	rotor outer diameter - Fig. 3
$D_{\rm stator}$	[mm]	131	stator inner diameter - Fig. 3
Vol	[cc]	1398	volume of the stator external packaging
B'_S	[mT]	22.5	B-field ripple magnitude - Eq.(29)

TABLE IV: Added energy depending on B'_S

Quantity		$Value$	Description
B'_S	[mT]	22.5	B-field ripple magnitude - outcome Table III
rpm	[rev/min]	1000	reference shaft rotational speed
$\textsc{max}\{d\phi'_S/d\phi\}$	[-]	0.244×10^{-3}	*a priory* assumption, or updated with Eq.(18)
Q'_S	[W/rad/s]	0.143×10^{-3}	energy increment per turn on shaft - Eq.(12)
P'_S	[W]	0.96	steady output power on shaft - Eq.(13)

It is worth noting that the quantities in Table III convey, independently of $\textsc{max}\{d\phi'_S/d\phi\}$, to the adopted best value for B'_S (for instance, a close match with $B_r(\varphi)$ for given gap). Afterwards, the assumed value for $\textsc{max}\{d\phi'_S/d\phi\}$ yields the calculated generated power P'_S for given rpm, as shown in Table IV. Therefore, final validation from measured values is readily possible.

In view of Table II, considering rpm = 1000, the ratio

$$(P'_S/\omega) = 9.17\times10^{-3}\ \text{[J/rad]}\ \text{ leads to }\ \textsc{max}\{d\phi'_S/d\phi\} = 0.244\times10^{-3}$$

in Table IV, calculated with (18). This numerical value is expected to remain essentially the same in similar design attempts, provided that the helical geometric proportions in Fig. 4 are maintained. For instance, while keeping rpm = 1000, the design procedure applied to other PM types results in calculated values :

- S-05-02-N52N, r_C = 35 mm, gap = 3 mm $\Rightarrow$ P'_S = 0.11 W
- S-10-05-N52N, r_C = 57 mm, gap = 6 mm $\Rightarrow$ P'_S = 0.96 W
- S-20-10-N(42), r_C = 112 mm, gap = 8 mm $\Rightarrow$ P'_S = 11.5 W

C. Details of the test platform

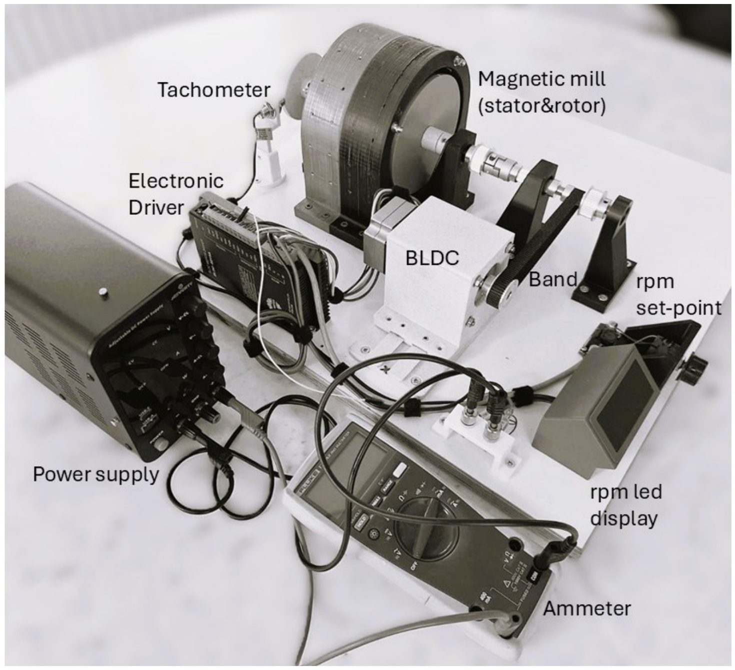

Fig. 13: Platform for testing a primal magnetic mill.

- Regulated power supply : JESVERTY SPS-3010V, 0-30VDC 0-10A, 24VDC constant voltage stability: $\leq 0.5\% + 3\mathrm{mV}$, ripple noise: $\leq 0.5\%$ VP-P
- BLDC : ACT Motor 57BLF03, 24VDC, 15A, 3000 rpm
- BLDC motor driver : BLDC-8015A, 24-50 VDC, rated 15A
- Ammeter : FLUKE 179, range 6 ADC, resolution 0.001 ADC, accuracy $\pm$(1.0% + 3)
- Tachometer : Hall sensor, 10-9999 rpm, accuracy $\pm 0.1\%$, reading ± 1 digit
- The driving belt from motor to rotor seems to be necessary to allow for small variations in rotation speed. Nevertheless, other types of coupling could be considered as research topic.

VII. Conclusion

In this report, we present a relatively simple concept intended to explore the essential functionality of a primal magnetic mill, namely the generation of mechanical power without reliance on conventional energy sources. Measurements performed with accurate instrumentation reveal that, when comparing the energy performance of the test system operating with a mill without and with the stator, respectively, there is a *consistent* positive difference in the total electrical power input. In other words, under equivalent operating conditions, the test system with the fully assembled mill requires less energy input than the incomplete configuration without the stator, which is interpreted here as evidence of excess energy generation by the mill.

To place these findings within a theoretical framework, we also propose a vibrational model for the analysis and design of the primal mill. In our view, this model may facilitate the independent reproduction, investigation, and validation of the reported results.

Acknowledgments

The personal communications with Horst Eckardt and Renato Barros Costa were greatly appreciated. The author gratefully acknowledge the financial support provided by Leo Gerris, which enabled the development of the prototypes presented in this research. The author also would like to express his gratitude to Woulter van der Most for the design and implementation of the prototypes and test setup.

References

[1] Dicas do Leão (anonymous author), first appeared in Feb. 2023,
https://www.youtube.com/watch?v=SswB3mj1XIY
Archived demonstration videos in mp4 format:
https://github.com/JLDuarte55/magnetogenesis

[2] H. Eckardt, *ECE UFT - The Geometrical Basis of Physics, Vol. I - Classical Physics*, textbook, epubli, Berlin, 2022, freely available as UFT Paper 438, Unified Field Theory (UFT) section of *https://aias.institute*.

[3] J.L. Duarte, *Essay on magnetic-wind mills - Part III*, TU Eindhoven Research Report, Dec. 10, 2024
https://research.tue.nl/en/publications/essay-on-magnetic-wind-mills-parts-i-ii-iii

[4] J.L. Duarte, *Kure Tekko magnet Wankel motor reexamined*,
AIAS - Publications - Electromagnetic ECE Theory, Oct. 2025
https://aias.institute/3-Scientific-Work/Publications.html

[5] E. Durand, *Magnétostatique*, Masson et Cie., 1968.